Applied Catalysis B: Environment and Energy 344 (2024) 123621

Contents lists available at ScienceDirect

Applied Catalysis B: Environmental

journal homepage: www.elsevier.com/locate/apcatb

High conductive polymer PANI link Bi_2MoO_6 and PBA to establish "tandem hybrid catalysis system" by coupling photocatalysis and PMS activation technology

Aiwen Wang [a], Rui Wang [a], Yunhao Pan [a], Jiaxin Ni [a], Xiongying Liang [a], Meng Du [a], Jun Zhang [a], Dongmei Liu [a,*], Jun Ma [a], Jing Wang [b,c,**], Wei Wang [a,*]

[a] State Key Laboratory of Urban Water Resource and Environment (SKLUWRE), School of Environment, Harbin Institute of Technology, Harbin 150090, PR China
[b] Institute of Environmental Engineering, ETH Zürich, Zürich 8093, Switzerland
[c] Laboratory for Advanced Analytical Technologies, Empa, Swiss Federal Laboratories for Materials Science and Technology, Dübendorf 8600, Switzerland

ARTICLE INFO

Keywords:
Photocatalysis
Peroxymonosulfate
Tandem hybrid catalysis system
Bi_2MoO_6/PBA
Highly conductive PANI

ABSTRACT

In order to design an efficient advanced oxidation system to improve the inherent limitations in removing refractory organic pollutants, we couple photocatalysis and peroxymonosulfate (PMS) activation technology to establish a tandem hybrid catalysis system inspired by series hybrid electric vehicles. Among them, Bi_2MoO_6, as an electric power source, can be driven by fuel (light) to generate continuous power (electron) input into the prussian blue analogues (PBA) through the transmission shaft polyaniline (PANI), allowing it to respond quickly and continuously activate PMS. Therefore, it exhibits excellent catalytic performance to degrade DC increased by 55%, and the catalytic rate constant k increased by 7 times compared with the PMS alone. Continuous flow experiments are explored to reveal the feasibility of engineering applications. This study provides a new strategy of tandem hybrid catalysis system to drive future advanced water treatment technologies.

1. Introduction

Antibiotics are commonly used for the prevention and treatment of infectious diseases, and the self use of antibiotics has increased since the outbreak of the COVID− 19 crisis [1]. The potential threat of antibiotic residues has led to an urgent need for reliable and environmentally friendly new treatment technologies [2,3]. The advantages of photocatalytic technology for water treatment have been proven [4,5]. Photons with energy higher than the bandgap are absorbed by semiconductor catalysts and excited to form electrons (e^-) and holes (h^+) with strong redox ability [6–9]. However, the presence of natural organic matter (NOM), carbonates, and other background components significantly limits the effectiveness of photocatalytic processes by clearing reactive oxygen species (ROS) and light [10]. Although the fields of materials and engineering sciences have been striving to improve photocatalytic efficiency, there are still inherent limitations in the application of new research in actual water treatment systems [11]. The advanced oxidation process (AOPs) of peroxymonosulfate (PMS) for water treatment has undergone a long development in the removal of refractory organic pollutants [12–14]. PMS can generate ROS through various transition metal ions activation to oxidize pollutants into harmless small compounds [15–18], thus it has strong adaptability and efficiency over a wide pH range. In addition, as a typical sulfate oxidant, PMS is widely used for its chemical stability and ease of transportation and storage [19–21]. However, it is difficult to produce ROS for the degradation of most organic substances using PMS alone, and metal catalysts pose a potential threat of ion leakage [22,23]. Therefore, it is necessary to find a green and fast technology for activating PMS.

Electron transfer is the key to PMS activation and ROS generation in this PMS activation process. It is found that the activation performance of PMS can be accelerated by introducing photocatalysis to increase the electron generation rate in the system [24–26]. Many academic studies focus on material development, including complex preparation methods and reaction processes, neglecting the improvement of water treatment system performance through innovative technological design [27]. Therefore, the development of low−cost innovative reactors has important scientific significance and application prospects. Imagine a stationary image of a car on the road, is it moving forward or reversing?

* Corresponding authors.
** Corresponding author at: Institute of Environmental Engineering, ETH Zürich, Zürich 8093, Switzerland.
E-mail addresses: ldm819@126.com (D. Liu), jing.wang@ifu.baug.ethz.ch (J. Wang), wangweirs@hit.edu.cn (W. Wang).

https://doi.org/10.1016/j.apcatb.2023.123621
Received 22 September 2023; Received in revised form 6 December 2023; Accepted 11 December 2023
Available online 16 December 2023

Only by checking the subsequent images, the direction of the car can be predicted. We were inspired by hybrid electric vehicles (SHEVs): there were two power sources—electric power sources (motors) and thermal power sources (traditional gasoline engines), that could strengthen their respective advantages and complement their respective weaknesses, thereby improving overall vehicle efficiency [28,29].

Here, a tandem hybrid catalysis system was constructed by loading Bi_2MoO_6 and PBA onto porous light−permeable sponge skeleton through the coating of PANI (BiM−PBA@PLS). Three dimensional (3D) materials have a large specific surface area and layered pore structure, which are more conducive to the adsorption of organic pollutants and electron transport during AOPs [30–32]. Among them, PANI couples the photocatalysis and PMS activation technology with its widely delocalized π–conjugated electron system. In the system, the fuel (light) excited electrical power source (Bi_2MoO_6) to continuously input power (electrons) into the thermal power source (PBA) through the drive shaft (PANI), which enables it to respond quickly and sustain PMS activation. Therefore, BiM−PBA@PLS showed high removal ability for DC degradation. Moreover, traditional powder catalysts can be fixed on support carriers without the need for ultrafiltration separation, making it convenient for recycling [33,34]. We also investigated continuous flow scale experiments by constructing a reactor to reveal the feasibility of its industrial application. There is reason to believe that BiM−PBA@PLS, which is easy to prepare and has strong cycling ability, can significantly promote innovation in water treatment technology of solar driven tandem hybrid catalysis system, and is of important significance for the advancement of cost-effective wastewater treatment and catalytic technology.

2. Materials and methods

All the chemical reagents used in this work to prepare catalysts and evaluate the activity of tandem hybrid catalysis system were commercially available and detailed in Text S1. The detailed preparation method of BiM−PBA@PLS could be found in Text S2. In brief, Bi_2MoO_6 (BiM) photocatalyst and CoFe–PBA (PBA) transition metal catalyst were prepared by typical solvothermal and chemical deposition method respectively, and then PANI gel riveted Bi_2MoO_6 and PBA were used on the porous light−permeable sponge to construct BiM−PBA@PLS. The catalytic activity of the BiM−PBA@PLS tandem hybrid catalysis system was systematically studied through light irradiation conditions and activation PMS experiments for the DC degradation. The mechanism of coupling photocatalysis and PMS activation was described in detail in the support information through the characterization methods in Text S3, the experimental methods in Text S4, and the DFT calculation in Text S5.

3. Results and discussion

3.1. Morphological and catalytic characteristics of BiM−PBA@PLS

The synthesis of BiM−PBA@PLS was carried out using previous research methods to prepare Bi_2MoO_6 and PBA, respectively [16,35]. Specific descriptions were provided in Fig. 1a and Text S2. In brief, PANI, with its widely delocalized π-conjugated electron system, served as the conductive and adhesive substrate that riveted Bi_2MoO_6 and PBA on the sponge during the construction of the tandem hybrid catalysis system. The encapsulation of a small amount of PANI could transfer electrons generated by Bi_2MoO_6 to PBA, while also making photo generated carriers easier to be migrated for catalytic reactions [36]. PANI solution had a strong gel tendency even at very low concentrations due to its strong interactions between molecular chains [37], so the catalyst could be coated on the sponge surface through its gelation. The effective diffraction peak crystal structure of the synthesized Bi_2MoO_6, PBA, PANI and BiM−PBA@PLS could be observed in the Fig. S1, and Bi_2MoO_6 and PBA had layered spherical and cubic structures, respectively, as observed in Fig. S2. Fig. 1b showed the FTIR characteristic spectra of the composite material, with the main characteristic wavelengths in Table S1. The strong absorption peaks of PANI at approximately 1574 and 1484 cm^{-1} were attributed to the stretching vibration

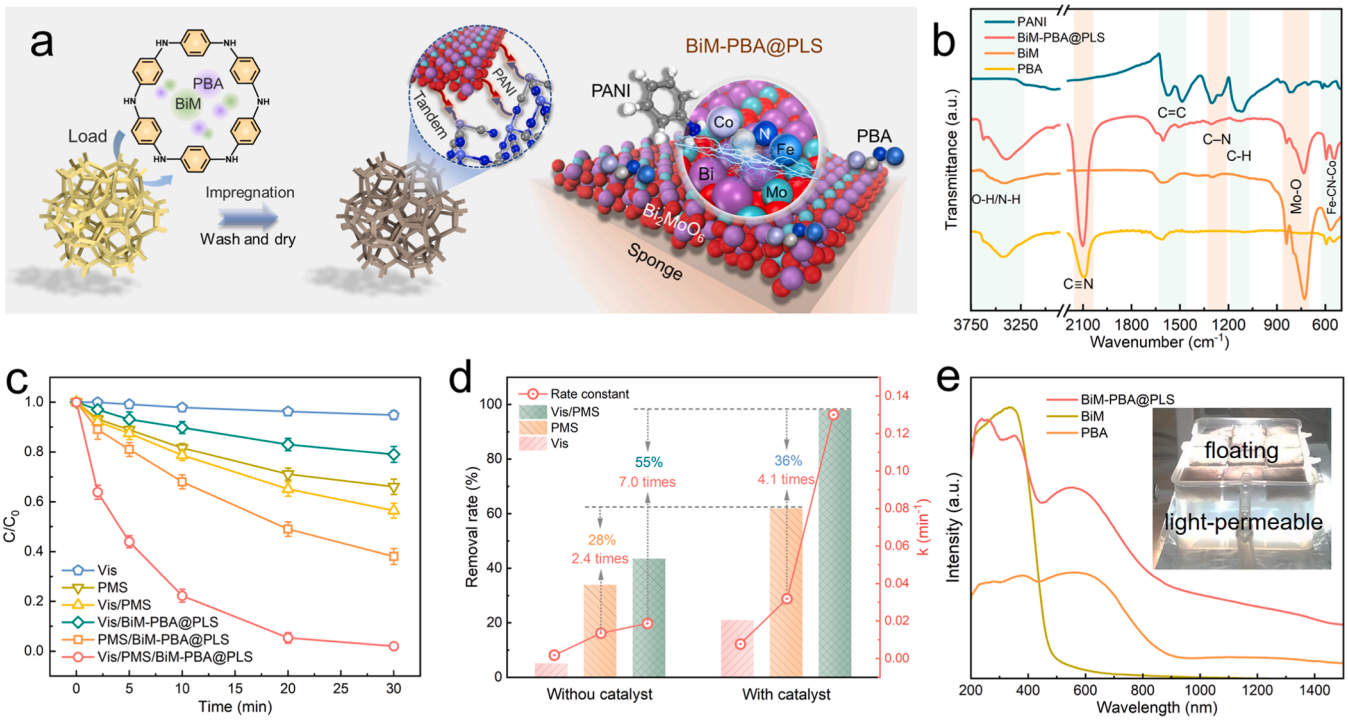

Fig. 1. (a) Synthesis schematic illustration. (b) FITR spectra of as–prepared catalysts. (c) Catalytic degradation curve of catalysts for DC and (d) relationship between degradation curves and apparent reaction rate constant k on photoexcitation. Reaction Conditions: [DC] = 10 mg L^{-1}, [volume] = 50 mL, [PMS] = 0.325 mM. (e) UV–vis diffuse reflectance spectra of catalysts, the inset is the photos of the floating and light−permeable reactor.

peaks of C=C quinone and benzene type rings. The 1299 cm^{-1} peak was attributed to C−N stretching of aromatic secondary amines, and the 1134 cm^{-1} peak was related to the plane stretching of C−H on the benzene ring [38]. For Bi_2MoO_6, the peaks at 810 and 730 cm^{-1} could be attributed to the stretching and asymmetric stretching vibration of the Mo−O bond in MoO_6 [39]. In addition, BiM−PBA@PLS exhibited characteristic peaks corresponding to the functional groups of PANI and Bi_2MoO_6, as well as the peaks of CoFe−PBA at 593 and 551 cm^{-1} of Fe−C≡N − Co, confirming the successful encapsulation of Bi_2MoO_6 and PBA by PANI on the sponge surface.

The performance differences between coupling photocatalysis and PMS activation technology in tandem hybrid catalysis system were investigated using DC as a pollutant. It could be found that the degradation efficiency was poor when only treated with photocatalysis, and the removal efficiency was only about 65% within 150 min (Fig. S3a). When PBA and BiM−PBA@PLS were added to the PMS system, the degradation efficiency was improved (Fig. S3b), due to the PMS activation by Co and Fe of PBA. In addition, the adsorption capacity of as–prepared catalysts could be found to be negligible. However, the tandem hybrid catalysis system (Vis/PMS/BiM−PBA@PLS) showed strong advantages (Fig. 1c). The removal rate and catalytic rate constant k of BiM−PBA@PLS activated PMS for DC degradation increased by 28% and 2.4 times. In the photocatalytic coupled PMS activation system (Vis/PMS), the ability of BiM−PBA@PLS to degrade DC increased by 55%, and the catalytic rate constant k increased by 7 times. Compared with the absence of photocatalysis, the removal rate increased by 36%, and the catalytic rate also increased by 4.1 times (Fig. 1d). Meanwhile, the removal rate of total organic carbon (TOC) at 30 min was 71% (Fig. S4), indicating its remarkable ability to mineralize DC. BiM−PBA@PLS had advantageous rate constant k (min^{-1}) compared to other reported catalysts for DC degradation of photocatalysis or PMS activation (Table S2). The above experimental results indicated that the intervention of photocatalytic technology in a tandem hybrid catalysis system altered the traditional PMS activation process and catalytic reaction mechanism. Therefore, the photoresponse performance of the catalyst was explored through UV–vis diffuse reflectance spectra (DRS). In Fig. 1e, it could be seen that BiM−PBA@PLS was light−permeable and could float on the water surface. This was because of the considerable pore size of the sponge, which facilitates multiple refractions of light within it, leading to more light absorption and providing favorable conditions for photocatalytic reactions (Fig. S5 and S6). The enhancement of the Vis−NIR optical region of BiM−PBA@PLS might be due to the photosensitivity exhibited by PBA at 900 nm.

3.2. Exploration of electron transfer mode by PANI tandem

The effective absorption of light by semiconductors to induce the excitation and migration of charge carriers was the key to activating PMS. The scanning electron microscope (SEM) images in Fig. 2a could reveal the morphological changes of the sponge before and after wrapping Bi_2MoO_6 and PBA with PANI. The adhesion of granular materials on the surface of BiM−PBA@PLS was strong evidence for the Bi_2MoO_6 and PBA existence. The encapsulation of PANI was not only to wrap the catalyst on the sponge, but also the key to constructing a tandem hybrid catalysis system. The electrochemical impedance spectroscopy (EIS) in Fig. 2b showed that individual sponge had poor conductivity, while loading only Bi_2MoO_6 and PBA could not improve. Surprisingly, the coating of PANI significantly increased the conductivity of the sponge evidenced by its minimal arc radius of the Nyquist plot in EIS. This was because the electrons were difficult to transfer between two separate catalysts due to spatial distance (Fig. 2c) [40]. However, the two catalysts were connected in tandem by PANI and established high−rate carrier transfer channels for them. The successful establishment of the channel could be clearly observed through the mapping and high−resolution TEM (HR–TEM) in Fig. 2d and S7, which showed the Bi and Mo elements of Bi_2MoO_6, and the Co and Fe elements of PBA, as well as the C and N elements fully encapsulated by PANI on the sponge. Nanosheets of Bi_2MoO_6 with (200) lattice stripes (0.28 nm) could be seen inserted in the interfaces of PBA with more disorganized lattice as well as structures wrapped by amorphous PANI [41]. In addition, density functional theory (DFT) calculations were introduced to explore electron transfer pathways and mechanisms. As shown in the differential charge distribution in Fig. 2e, PANI exhibited strong interactions at the interface between Bi_2MoO_6 and PBA. The calculated work function in

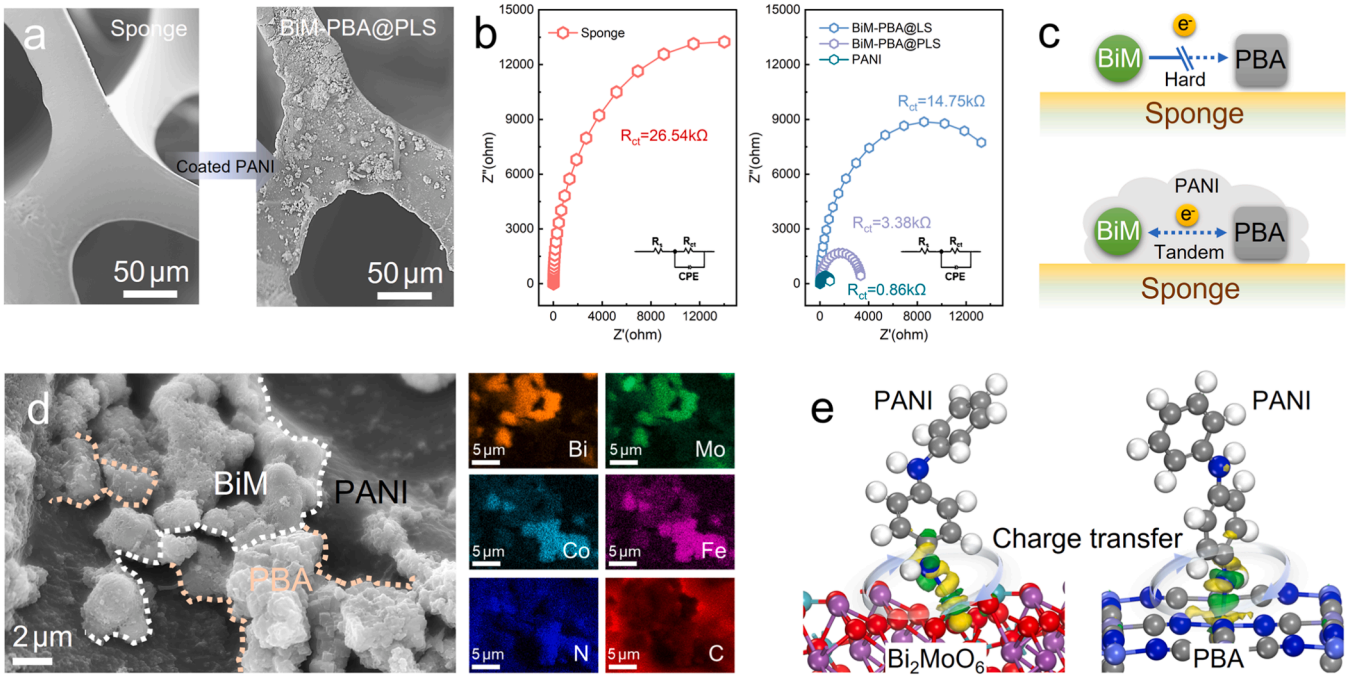

Fig. 2. (a) SEM image, (b) EIS Nyquist plots and (d) element mapping of BiM−PBA@PLS. (c) Schematic illustration of high conductive PANI tandem Bi_2MoO_6 and PBA. (e) Electron transfer at the interface between PANI and catalyst with charge accumulation in green and depletion in yellow.

Fig. S8 could prove that the potential difference between PANI and catalysts led to more electron transfer and accumulation [42]. The charge carriers generated by the catalyst circulated continuously between PANI layers and participated in catalytic reactions, thereby suppressing the consumption of electron return with hole.

Further exploration of the pathways and directions of electron transfer in photoexcited tandem hybrid catalysis system was important to identify the active centers of PMS activation. The work function (Φ) was determined by UPS as shown in Fig. 3a. The Φ of Bi_2MoO_6 and PBA were estimated to be 4.63 and 5.69 eV, which was also consistent with DFT calculations. The energy level difference between them led to the inevitable occurrence of electron transfer at the contact interface [43]. Therefore, X − ray photoelectron spectroscopy (XPS) had been applied to analyze the valence state changes and catalytic mechanism of the tandem hybrid catalysis system. Specifically, the electrons on the Bi_2MoO_6 side transferred to the PBA interface, leading to electron depletion and a slight positive shift in the peaks of Bi 4 f and Mo 3d due to the high Fermi level of Bi_2MoO_6 (Fig. 3b). On the contrary, the Co 2p and Fe 2p of PBA exhibited slight negative shifts due to electron acceptance. However, in alone PMS activation system (without light), the electron of BiM−PBA@PLS was transferred to PMS for activation, and it led to the loss of electrons in Bi_2MoO_6 and PBA, resulting in a slight positive shift of the XPS peak and an increase in the proportion of Co^{3+} and Fe^{3+} peak area. In the photocatalytic synergistic PMS system, the photogenerated electrons generated by photoexcitation of Bi_2MoO_6 were continuously supplied to PBA, which led to stable operation of the tandem hybrid catalysis system and PBA system electron density increase, resulting in a relative negative shift of the XPS peak. As shown in the schematic diagram of carrier transfer in Fig. 3c, the electrons in Bi_2MoO_6 transitioned from the valence band (VB) to the conduction band (CB) after excited by light. Due to the high−rate carrier transfer channel provided by the PANI encapsulation, electrons were preferentially transferred to suppress carrier recombination (Fig. S9). PANI, as a transit station, transferred most of the electrons to PBA due to their intimate interface and work function, achieving charge carrier cycling between Bi_2MoO_6 and PBA. The chronoamperometric and

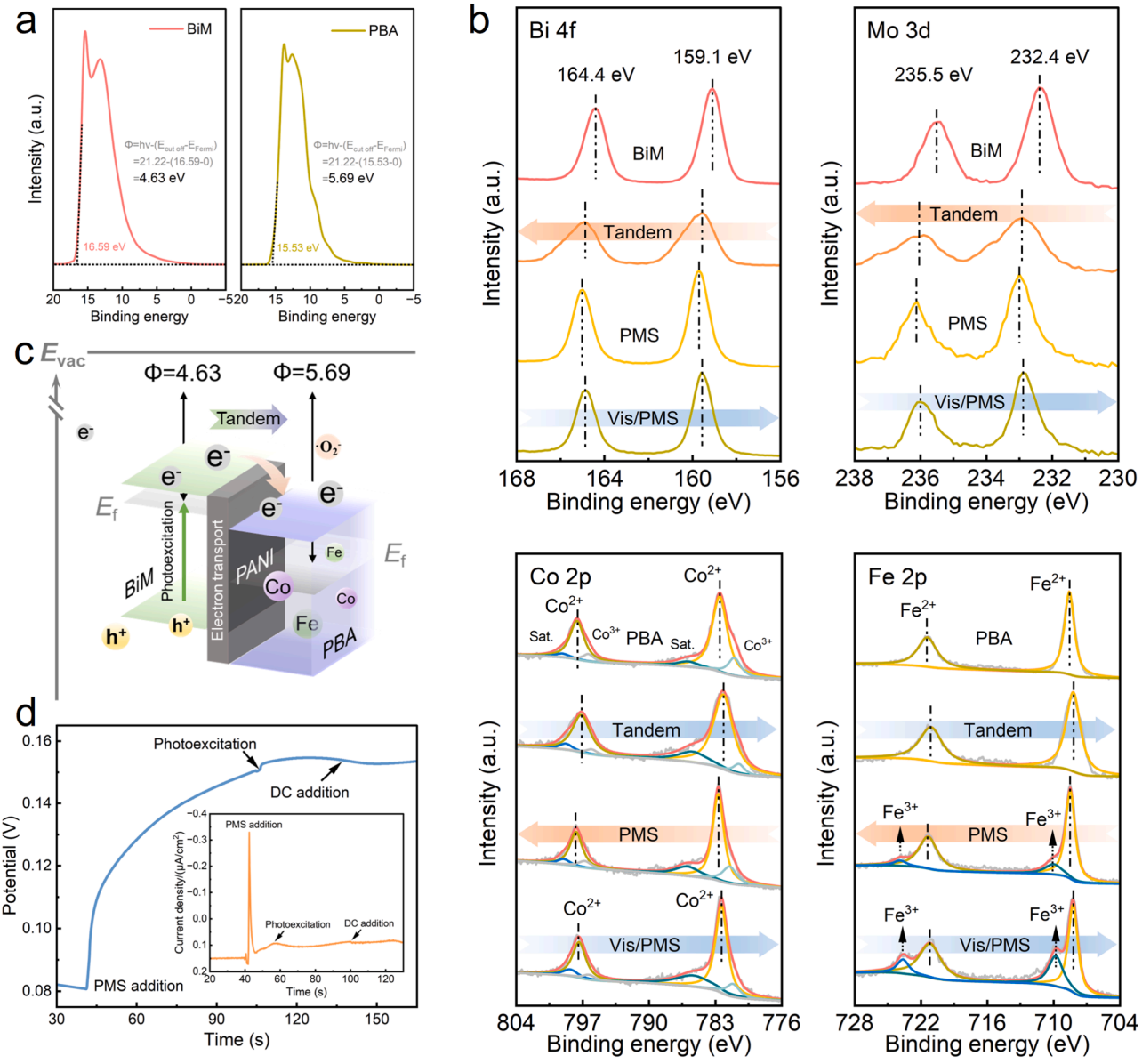

Fig. 3. (a) UPS spectrum of BiM and PBA, (b) The high−resolution XPS spectra of as−prepared catalysts before and after PMS or Vis/PMS tests. (c) Schematic illustration of tandem hybrid catalysis system by BiM−PBA@PLS. (d) Chronopotentiometry and chronoamperometry (inset) curve of charge carrier cycle reactor with adding PMS, photoexcitation and DC.

chronopotentiometry curve analysis also demonstrated the electron transfer mechanism between the tandem hybrid catalysis system and DC (Fig. 3d). The sharp increase in output potential and current with the PMS addition indicated that the exchange of electrons at the PMS and BiM−PBA@PLS catalytic sites. The redox potential intensity further increased after photoexcitation Bi_2MoO_6, indicating the enhancement effect of the tandem hybrid catalysis system. Meanwhile, the decrease in current and potential proved the progress of catalytic DC reaction. Therefore, tandem hybrid catalysis system had changed the traditional transition metal redox reaction pathway. Among them, the high conductivity of PANI had a significant impact on electron transfer kinetics, which was a powerful driving force for promoting the separation of photogenerated carriers [44]. It was convincing that the introduction of PANI established transfer channels for interlayer charge to enhance the DC catalytic degradation.

3.3. Evaluation of catalytic site and mechanism

The general catalytic reaction involved the following steps: PMS was captured by the catalyst to form a surface complex, which is then activated to generate ROS. However, the tandem hybrid catalysis system involved photoexcitation of Bi_2MoO_6 to generate charge carriers, which were then separated and transported by PANI for continuous supply to PBA to enable PMS activation. Therefore, only a small amount of PMS (0.98 mM) was needed to remove 10 mg L^{-1} of DC, and the removal rate reached over 98% within 10 min with a catalytic rate constant of 0.362 min^{-1} (Fig. S10a), and the removal rate was above 88% using 0.325 mM PMS even at a DC concentration of 20 mg L^{-1} (Fig. S10b−c). Meanwhile, PANI coated on the sponge surface could also significantly inhibit the leakage of metal ions due to the strong interaction between their chains, which has a strong gel tendency [37] (Fig. S11 and Table S3). Fig. S12 showed the effect of pH on the DC degradation in tandem hybrid catalysis system. In an aqueous solution with $pH_{initial}$ = 3.03, PMS was more stable and difficult to activate due to the abundance of H^+ ions [45]. However, the degradation ability of BiM−PBA@PLS on DC was significantly improved when the $pH_{initial}$ was higher than 5.15. Exploring the interaction mechanism between PMS and BiM−PBA@PLS through Zeta potential (Fig. 4a). The pK_{a1} and pK_{a2} of PMS were 0 and 9.4, respectively, thus, PMS existed in the anionic form of HSO_5^- over a wide pH range. However, the tandem hybrid catalysis system had a pH_{final} from 2.9 to 4.4 in a wide initial pH range, which was lower than the pH_{IEP} = 5.96 of BiM−PBA@PLS (Fig. 4b). Therefore,

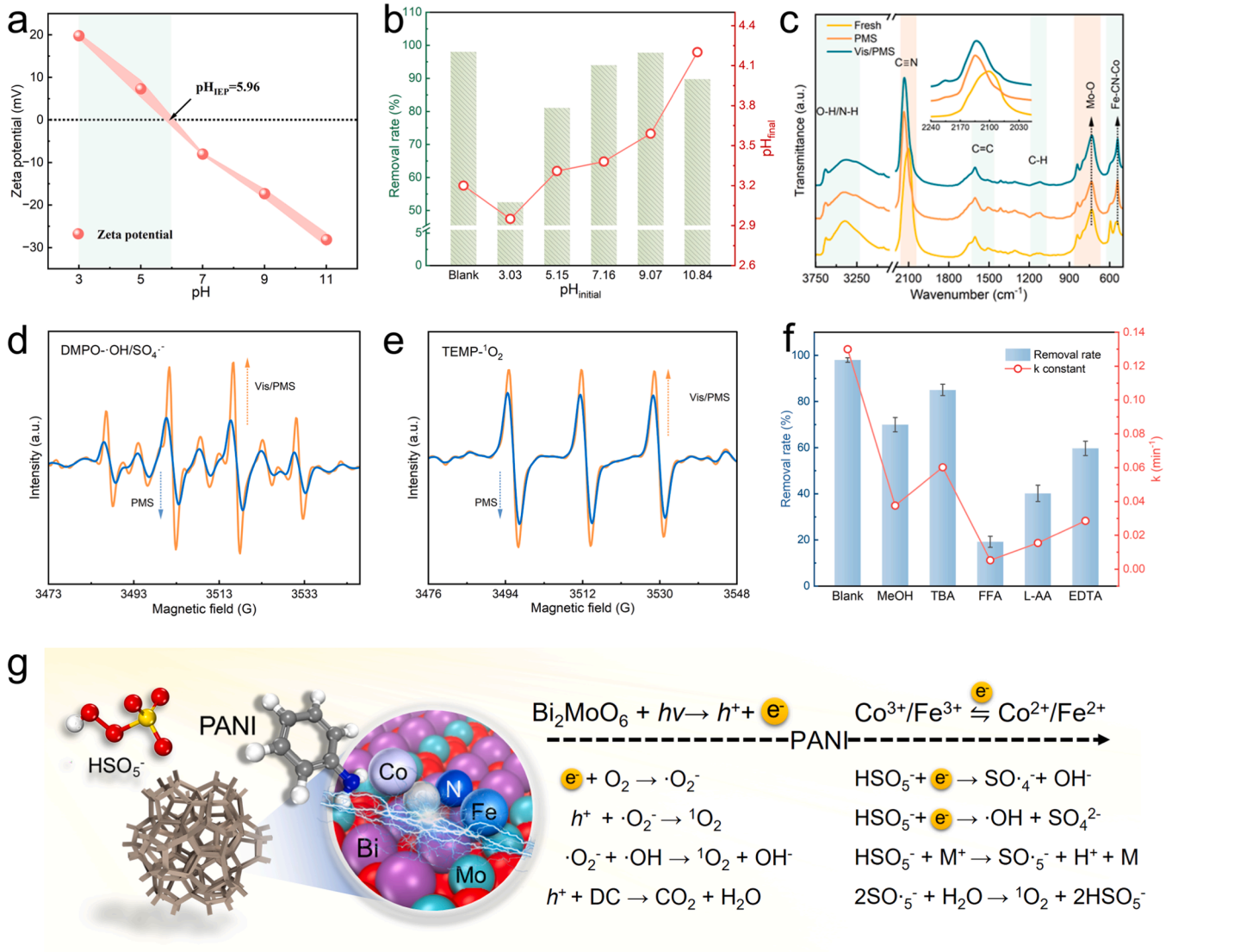

Fig. 4. (a) Zeta potential of BiM−PBA@PLS. (b) The degradation of DC and pH_{final} at different $pH_{initial}$. (c) The FTIR spectra of BiM−PBA@PLS before and after PMS or Vis/PMS tests. EPR signals for (d) DMPO−•OH/SO_4•$^-$and (e) TMPO−$^1O_2$. (f) Scavenger quenching tests. (g) Mechanism schematic diagram of the tandem hybrid catalysis system for synergistic DC degradation.

HSO_5^- could easily be complexed by positively charged BiM−PBA@PLS through electrostatic attraction. The Fe−C≡N − Co peak of PBA had a certain shift or superposition enhancement observed in the FTIR spectrum after the catalytic reaction (Fig. 4c). This was because the PBA structure contained a certain amount of open channels formed by unbranched nitroso group and coordinated water molecules [46,47], which was demonstrated in the electron paramagnetic resonance (EPR) (Fig. S13). Therefore, the isomerization of CN bonds and multiple changes in the valence states of metal centers led to peak shift of Fe−C≡N − Co during the catalytic process [41,48]. In addition, the active radicals generated in the tandem hybrid catalysis system were identified by EPR. As shown in Fig. 4d and e, the characteristic peaks of the 1:1:1 triplet signal of TEMP−$^1O_2$ and DMPO−SO_4•$^-$/•OH were identified, demonstrating the generation of $^1O_2$, SO_4•$^-$, and •OH in the system. It was worth noting that the ability to generate ROS was significantly improved after photocatalytic intervention, which provided strong evidence for the synergistic enhancement of photocatalytic coupling PMS activation. The results of quenching test indicated that the degradation of DC involved the participation of various active substances (Fig. 4f). Interestingly, $^1O_2$, •O_2^-, and h^+ contributed significantly, while •OH/SO_4•$^-$ assisted in degradation process. The •O_2^- could be oxidized to $^1O_2$ or disproportionated to $^1O_2$ by h^+, resulting in $^1O_2$ through electron transfer [49]. In tandem hybrid catalysis system, the Bi_2MoO_6 of BiM−PBA@PLS could be excited by light to generate •O_2^- due to its CB and VB position (Fig. S14), and also serve as an electron donor for PBA and PMS to generate ROS. Due to the presence of multiple free and non−free radicals in the system, BiM−PBA@PLS had a certain degradation ability against all 8 antibiotics (sulfonamides: SA, SMX and SDZ, tetracyclines: TC, DC, OTC and CTC, and quinolones: levofloxacin LVF), with a better degradation rate for tetracyclines (Fig. S15). Therefore, the mechanism of DC degradation in tandem hybrid catalysis system was summarized, including the photocatalytic coupling PMS activation process (Fig. 4g). Firstly, HSO_5^- was captured to form a surface complex through electrostatic attraction. At the same time, the photogenerated electrons generated by Bi_2MoO_6 were transferred to the PBA in tandem through the PANI high−rate carrier transfer channel, causing the cycle of $Co^{3+}/Fe^{3+} = Co^{2+}/Fe^{2+}$ and accelerating the regeneration of Fe^{2+}/Co^{2+}, continuously providing energy for PMS

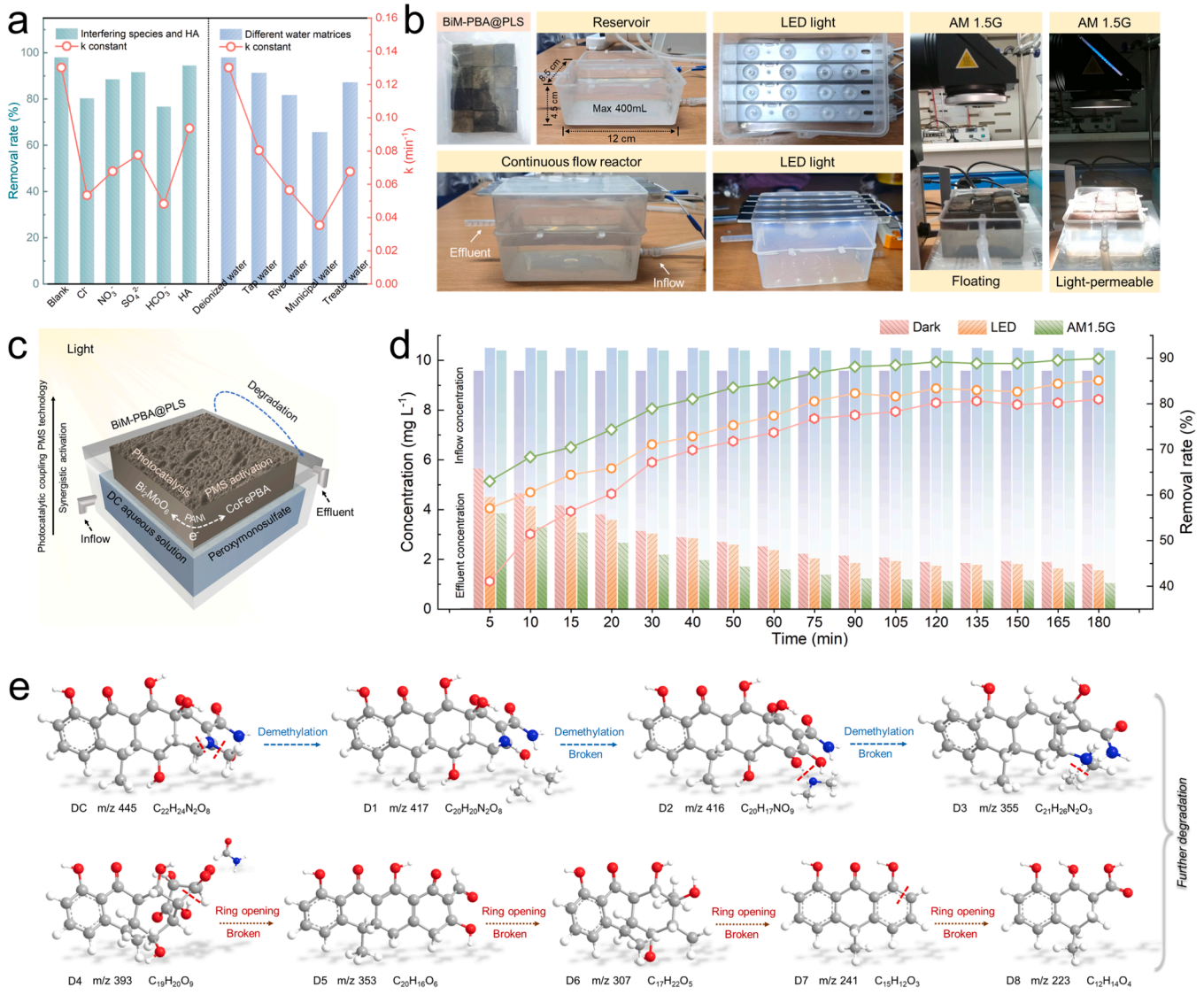

Fig. 5. (a) Effects of different anions Cl^-, NO_3^-, SO_4^{2-}, HCO_3^-, (10 mM) and HA (2 mg L^{-1}), and water matrices (Harbin, China) on the DC degradation. (b) Photo of the photoexcitation continuous flow reaction equipment. (c) Schematic diagram of the tandem hybrid catalysis system reactor. (d) Performance of BiM−PBA@PLS in continuous flow reactions under different illuminant. (Reaction conditions: The reservoir was pre−filled with 380 mL with 10 mg L^{-1} of DC solution, then 10 mg L^{-1} DC and 0.2 g L^{-1} PMS were injected into the bottom of the device at a flow rate through a pump. Samples were collected when the water flowed out from the top of the device). (e) The possible pathways for DC degradation by BiM−PBA@PLS under Vis/PMS.

activation. It significantly promoted the generation of $^1O_2$, $SO_4\bullet^-$, and •OH (Fig. 4g) [30], until DC was rapidly degraded through both free and non−free radicals.

3.4. Potential application of the tandem hybrid catalysis system

Humic acid (HA) and inorganic anions such as Cl^-, HCO_3^-, NO_3^-, and SO_4^{2-} were common in wastewater. The influence of water quality components on the DC catalytic performance was shown in Fig. 5a. Among anions, HCO_3^- had the biggest impact on DC degradation, while Cl^- had a more unfavorable effect than other anions (SO_4^{2-} and NO_3^-). Because the pH value of the aqueous solution could be increased by HCO_3^-, it inhibited the catalytic reaction (Fig. 4b) [8]. In addition, the influence of various ions was also attributed to the differences in reaction kinetics between active substances and anions. Cl^- and HCO_3^- could quench $SO_4\cdot^-$ and·OH or directly consume PMS, forming active radicals that could not effectively oxidize DC, such as Cl•, $Cl_2\bullet^-$ and ClO•, as well as $CO_3\cdot^-$ and $HCO_3\cdot$, thereby inhibiting the degradation process of DC [50]. The catalytic reaction was not significantly affected by NO_3^-. HA, a complex organic molecule composed of aromatic groups and various functional groups, was widely presented in natural water. However, the degradation was slightly affected by HA, and previous studies had also found that the phenolic groups of HA might had the role of electron donors [51]. Therefore, the catalytic degradation of DC in urban water was severely inhibited due to the interference of organic and inorganic substances (Fig. 5a). These results indicated that the tandem hybrid catalysis system of photocatalytic synergistic PMS activation technology was more suitable for the AOPs of antibiotics in the later stage of water treatment. The difference in DC degradation by three types of simulated light was to investigate the influence of different light sources on the tandem hybrid catalysis system (Solar−AM 1.5 G, LED−8 W, Visible light−420 nm cut) (Fig. S16). It could be found that the system exhibited the best DC degradation efficiency under simulated sunlight, due to the stronger excitation energy and effective utilization of full spectrum by Bi_2MoO_6, resulting in more photogenerated carriers compared to visible light. Meanwhile, the thermal energy generated by infrared irradiation was also beneficial for molecular diffusion and PMS decomposition (endothermic reaction) [52]. The tandem hybrid catalysis system still exhibited significant DC degradation performance under white LED compared to using it alone as a PMS activator. The combination of materials science and reactor engineering might present opportunities to improve water treatment performance. To explore the applicability of the dynamic equipment equipped with the tandem hybrid catalysis system that could sustainably handle a large amount of polluted water in the future, we assembled a continuous flow reactor as shown in Fig. 5b, including a water reservoir and a switchable light source. Due to the good floatability of BiM−PBA@PLS, it could be directly placed on the water surface of the reservoir without stabilization, which was conducive to the effective utilization of top light irradiation and promoted the synergistic activation PMS. At the bottom, fresh PMS and DC solution were pumped through a three-way valve to continuously catalyzed DC degradation, and then the solution was collected at the top to track the residual concentration (Fig. 5c). The results in Fig. 5d indicated that the efficiency of the alone PMS activation system was poor at 1 mL min^{-1}. DC content of 60% was directly leaked in the initial 5 min, and the stable removal efficiency reached about 80% after 120 min. Impressively, the reactor showed the best performance under simulated sunlight, reducing the initial concentration of DC from 10.4 to 3.8 mg L^{-1}, achieving a removal rate of 63% within 5 min and a stable maximum removal capacity of 90% within 90 min. It was worth noting that the tandem hybrid catalysis system reactor could still degrade 57% of DC within 5 min even under LED light, with a stable removal rate of 85% in 120 min. Meanwhile, considering cost and practicality [53], the tandem hybrid catalysis system reactor still had good performance under LED light with increased flow rate, and the reactor could operate continuously and stably for 24 h without attenuation compared to dark conditions (Fig. S17). The fragile sites on DC molecules were predicted using DFT calculation. As shown in Fig. S18 and Table S4, the Fukui electrophilic index (f^-) and the highest occupied molecular orbital (HOMO) sites N_{25}, C_{31}, C_{32}, and O_{22} of DC represented electron donors, making them more susceptible to attack through electrophilic reagents (h^+ and $^1O_2$) [35]. Sites with high radical index (f^0) values indicated susceptibility to $SO_4\cdot^-$ and·OH attacks (including N_{25}, O_{20}, C_7, and C_{14}) [54]. The nucleophilic index (f^+) and lowest unoccupied molecular orbital (LUMO) represented electron acceptance ability and indicated susceptibility to·O_2^- attack (nucleophilic reaction) in the hydroxyl functional group region (O_{20}, C_7, C_{14}, and C_2) [55]. The DC degradation products and pathway in the tandem hybrid catalysis system were further analyzed through HPLC−MS calculations (Fig. S19 and Table S5). Fig. 5e showed that the methyl region N_{25} easily loses electrons, allowing it to be attacked by h^+ and $^1O_2$, resulting in the generation of intermediate D1-D2 via bond breakage or demethylation. Subsequently, the hydroxyl functional group of O_{20} was attacked by·O_2^- to generate D3, and the molecular chain gradually broken and opened (D4-D6) to form a series of intermediate products by $SO_4\cdot^-$ and·OH (D7-D8), which were ultimately mineralized into H_2O and CO_2 [56]. Thus, Fig. S20 showed that the developmental toxicity of most intermediates was reduced. In addition, characterization analysis of BiM−PBA@PLS after continuous flow equipment reaction revealed that the catalyst on the sponge still had stable loading and crystal structure (Fig. S21). In short, the catalysts were coated on a sponge by highly conductive PANI, making it easy to recover and reuse while maintaining stability, reflecting the potential advantages of tandem hybrid catalysis system in improving persistent organic pollution in the actual environment.

4. Conclusions and outlook

In summary, we coupled photocatalysis and PMS activation technology to establish a 3D material of tandem hybrid catalysis system. In this system, photocatalysis technology was introduced into a floating light−permeable sponge to promote the charge carriers flow through highly conductive PANI. It serves as a bridge between the two technologies in tandem, breaking the energy barrier and providing driving force for photo generated carriers transfer at the sponge interface. The continuous migration of photogenerated charges of Bi_2MoO_6 into PBA altered the valence structure to synergistically activate PMS, accelerating the redox reaction and inducing the decomposition of DC through free/non free radical species. The experimental and theoretical simulation results analyzed the possible degradation pathways of DC, demonstrating remarkable stability of the tandem hybrid catalysis system and its suitability for AOPs in the later stage of water treatment.

This article provided a synergistic enhancement strategy to significantly improve the inherent shortcomings of photocatalysis and PMS activation technologies, such as the low efficiency of photocatalysis and the additional energy required for PMS activation, etc. Compared with other powder catalysts/co–catalysts, the preparation method of BiM–PBA@PLS was convenient and it had high cyclic utilization ability. In continuous flow experiments, the reactor was able to reduce the DC from 10.4 to 3.8 mg L^{-1}, with a removal rate of 63% within 5 min and a maximum removal rate stabilized at 90% within 90 min under simulated sunlight in continuous flow experiments. It was worth noting that the reactor could still degrade 57% of DC within 5 min even under LED light, with a stable removal rate of 85% in 120 min. Therefore, the tandem hybrid catalysis system in this study had promising application prospects in the field of water treatment. However, further exploration and optimization were needed for the subsequent regulation of the system and its application in actual water environments. At present, challenging and innovative water treatment technologies should be considered by sewage treatment plants to purify refractory organic matter. This work suggested that a tandem hybrid catalysis system might provide a new idea to address this limitation.

CRediT authorship contribution statement

Wang Aiwen: Writing – review & editing, Writing – original draft, Visualization, Validation, Software, Methodology, Investigation, Data curation, Conceptualization. **Wang Rui:** Software, Methodology, Data curation. **Pan Yunhao:** Visualization, Formal analysis. **Ni Jiaxin:** Visualization, Formal analysis. **Liang Xiongying:** Data curation. **Du Meng:** Visualization, Data curation. **Zhang Jun:** Formal analysis. **Liu Dongmei:** Writing – review & editing, Supervision, Project administration, Funding acquisition, Formal analysis, Conceptualization. **Ma Jun:** Investigation, Formal analysis. **Wang Jing:** Supervision, Project administration. **Wang Wei:** Funding acquisition, Formal analysis.

Declaration of Competing Interest

The authors declare that they have no known competing financial interests or personal relationships that could have appeared to influence the work reported in this paper.

Data Availability

Data will be made available on request.

Acknowledgements

We gratefully acknowledge the National Key Research and Development Program of China (2022YFC3005802), the National Natural Science Foundation of China (52070052), the State Key Laboratory of Urban Water Resource and Environment (Harbin Institute of Technology) (No. 2022TS16) and China Scholarship Council (202306120252). Additional thanks go to the High−Performance Computing Center, Harbin Institute of Technology.

Appendix A. Supporting information

Supplementary data associated with this article can be found in the online version at doi:10.1016/j.apcatb.2023.123621.

References

[1] Y. Hu, X. Wei, Q. Zhu, L. Li, C. Liao, G. Jiang, COVID-19 pandemic impacts on humans taking antibiotics in China, Environ. Sci. Technol. 56 (2022) 8338–8349.
[2] J. Leichtweis, Y. Vieira, N. Welter, S. Silvestri, G.L. Dotto, E. Carissimi, A review of the occurrence, disposal, determination, toxicity and remediation technologies of the tetracycline antibiotic, Process Saf. Environ. Prot. 160 (2022) 25–40.
[3] S. Yang, Y. Shi, X. Wang, Y. Liu, Y. Ren, W. Li, H. Zhang, X. Dai, W. Sun, B. Lai, Selective elimination of sulfonamide antibiotics upon periodate/catechol process: dominance of quinone intermediates, Water Res. 242 (2023), 120317.
[4] F. Yang, M. Du, K. Yin, Z. Qiu, J. Zhao, C. Liu, G. Zhang, Y. Gao, H. Pang, Applications of metal-organic frameworks in water treatment: a review, Small 18 (2022), 2105715.
[5] H. Liu, C. Wang, G. Wang, Photocatalytic advanced oxidation processes for water treatment: recent advances and perspective, Chem. – Asian J. 15 (2020) 3239–3253.
[6] F. Wang, J. Xu, Z. Wang, Y. Lou, C. Pan, Y. Zhu, Unprecedentedly efficient mineralization performance of photocatalysis-self-Fenton system towards organic pollutants over oxygen-doped porous g-C_3N_4 nanosheets, Appl. Catal. B: Environ. 312 (2022), 121438.
[7] S.L. Wang, Y. Zhu, X. Luo, Y. Huang, J. Chai, T.I. Wong, G.Q. Xu, 2D WC/WO_3 heterogeneous hybrid for photocatalytic decomposition of organic compounds with Vis–NIR light, Adv. Funct. Mater. 28 (2018) 1705357.
[8] J. Guo, H. Sun, X. Yuan, L. Jiang, Z. Wu, H. Yu, N. Tang, M. Yu, M. Yan, J. Liang, Photocatalytic degradation of persistent organic pollutants by Co-Cl bond reinforced CoAl-LDH/$Bi_{12}O_{17}Cl_2$ photocatalyst: mechanism and application prospect evaluation, Water Res. 219 (2022), 118558.
[9] Y. Jiang, Z. Xiong, J. Huang, F. Yan, G. Yao, B. Lai, Effective E. coli inactivation of core-shell ZnO@ZIF-8 photocatalysis under visible light synergize with peroxymonosulfate: efficiency and mechanism, Chin. Chem. Lett. 33 (2022) 415–423.
[10] J. Brame, M. Long, Q. Li, P. Alvarez, Inhibitory effect of natural organic matter or other background constituents on photocatalytic advanced oxidation processes: Mechanistic model development and validation, Water Res. 84 (2015) 362–371.
[11] S.K. Loeb, P.J.J. Alvarez, J.A. Brame, E.L. Cates, W. Choi, J. Crittenden, D. D. Dionysiou, Q. Li, G. Li-Puma, X. Quan, D.L. Sedlak, T. David Waite, P. Westerhoff, J.-H. Kim, The Technology Horizon for Photocatalytic Water Treatment: Sunrise or Sunset? Environ. Sci. Technol. 53 (2019) 2937–2947.
[12] Q. Zhong, C. Xu, Y. Liu, Q. Ji, Z. Xu, D. Sun, S. Zhou, B. Yang, Y. Dai, C. Qi, S. Yang, H. He, S. Li, C. Sun, Defect-engineered $FeSe_{2-x}$@C with porous architecture for enhanced peroxymonosulfate-based advanced oxidation processes, Appl. Catal. B: Environ. 309 (2022), 121259.
[13] C. Meng, B. Ding, S. Zhang, L. Cui, K.K. Ostrikov, Z. Huang, B. Yang, J.-H. Kim, Z. Zhang, Angstrom-confined catalytic water purification within Co-TiO_x laminar membrane nanochannels, Nat. Commun. 13 (2022) 4010.
[14] X. Xie, Y. Xiang, J. Cao, W. Dai, Z. Ao, H. Huang, X. Yang, F. Xiao, X. Ye, High-efficiency destruction of aromatic VOC mixtures in a MoS_2 cocatalytic Fe^{3+}/PMS reaction, Sep. Purif. Technol. 305 (2023), 122444.
[15] P. Xu, R. Wei, P. Wang, X. Li, C. Yang, T. Shen, T. Zheng, G. Zhang, $CuFe_2O_4$/diatomite actuates peroxymonosulfate activation process: Mechanism for active species transformation and pesticide degradation, Water Res. 235 (2023), 119843.
[16] A. Wang, J. Ni, W. Wang, D. Liu, Q. Zhu, B. Xue, C.-C. Chang, J. Ma, Y. Zhao, MOF Derived Co−Fe nitrogen doped graphite carbon@crosslinked magnetic chitosan Micro−nanoreactor for environmental applications: Synergy enhancement effect of adsorption−PMS activation, Appl. Catal. B: Environ. 319 (2022), 121926.
[17] Y.-J. Zhang, G.-X. Huang, L.R. Winter, J.-J. Chen, L. Tian, S.-C. Mei, Z. Zhang, F. Chen, Z.-Y. Guo, R. Ji, Y.-Z. You, W.-W. Li, X.-W. Liu, H.-Q. Yu, M. Elimelech, Simultaneous nanocatalytic surface activation of pollutants and oxidants for highly efficient water decontamination, Nat. Commun. 13 (2022) 3005.
[18] W. Wang, M. Chen, Catalytic degradation of sulfamethoxazole by peroxymonosulfate activation system composed of nitrogen-doped biochar from pomelo peel: Important roles of defects and nitrogen, and detoxification of intermediates, J. Colloid Interface Sci. 613 (2022) 57–70.
[19] C. Nie, Y. Hou, F. Liu, Q. Dong, Z. Li, P. Han, M. Tong, Efficient peroxymonosulfate activation by magnetic MoS_2@Fe_3O_4 for rapid degradation of free DNA bases and antibiotic resistance genes, Water Res. 239 (2023), 120026.
[20] G. Pan, J. Wei, M. Xu, J. Li, L. Wang, Y. Li, N. Cui, J. Li, Z. Wang, Insight into boron-doped biochar as efficient metal-free catalyst for peroxymonosulfate activation: Important role of -O-B-O- moieties, J. Hazard. Mater. 445 (2023), 130479.
[21] L. Xiao, Y. Deng, H. Zhou, F. Lu, C. Ke, Y. Ye, X. Pei, D. Xia, F. Pan, Activated carbon fiber mediates efficient activation of peroxymonosulfate systems: Modulation of manganese oxides and cycling of manganese species, Chin. Chem. Lett. 34 (2023), 108407.
[22] Q. Yang, H. Choi, S.R. Al-Abed, D.D. Dionysiou, Iron–cobalt mixed oxide nanocatalysts: Heterogeneous peroxymonosulfate activation, cobalt leaching, and ferromagnetic properties for environmental applications, Appl. Catal. B: Environ. 88 (2009) 462–469.
[23] X. Luo, Y. You, M. Zhong, L. Zhao, Y. Liu, R. Qiu, Z. Huang, Green synthesis of manganese–cobalt–tungsten composite oxides for degradation of doxycycline via efficient activation of peroxymonosulfate, J. Hazard. Mater. 426 (2022), 127803.
[24] A. Wang, M. Du, J. Ni, D. Liu, Y. Pan, X. Liang, D. Liu, J. Ma, J. Wang, W. Wang, Enhanced and synergistic catalytic activation by photoexcitation driven S−scheme heterojunction hydrogel interface electric field, Nat. Commun. 14 (2023) 6733.
[25] Y. Liu, F. Cun, D. Tian, P. Zhou, Y. Yuan, Z. Xiong, C. He, Y. Du, Z. Pan, B. Lai, Fast photo-Fenton-like oxidation in bismuth catalysis: a novel Fe(III) self-doped sodium bismuthate nanosheet, J. Hazard. Mater. 435 (2022), 128975.
[26] A. Wang, P. Zhou, D. Tian, H. Zhang, Z. Xiong, Y. Du, C. He, Y. Yuan, T. Chen, Y. Liu, B. Lai, Enhanced oxidation of fluoroquinolones by visible light-induced peroxydisulfate: The significance of excited triplet state species, Appl. Catal. B: Environ. 316 (2022), 121631.
[27] T. Van Gerven, G. Mul, J. Moulijn, A. Stankiewicz, A review of intensification of photocatalytic processes, Chem. Eng. Process.: Process.Intensif. 46 (2007) 781–789.
[28] L. Di Cairano, W. Bou Nader, M. Nemer, A simulation and experimental study of an innovative MAC/ORC/ERC system: ReverCycle with an ejector for series hybrid vehicles, Energy 230 (2021), 120830.
[29] M. Kebriaei, A.H. Niasar, B. Asaei, Hybrid electric vehicles: an overview, Int. Conf. Connect. Veh. Expo. (ICCVE) 2015 (2015) 299–305.
[30] L. Zhu, J. Ji, J. Liu, S. Mine, M. Matsuoka, J. Zhang, M. Xing, Designing 3D-MoS_2 sponge as excellent cocatalysts in advanced oxidation processes for pollutant control, Angew. Chem. Int. Ed. 59 (2020) 13968–13976.
[31] W. Qu, Z. Tang, W. Liu, Y. Liao, Y. Huang, D. Xia, Q. Lian, S. Tian, C. He, D. Shu, Self-accelerating interfacial catalytic elimination of gaseous sulfur-containing volatile organic compounds as microbubbles in a facet-engineered three-dimensional BiOCL sponge fenton-like process, Environ. Sci. Technol. 56 (2022) 11657–11669.
[32] J. Li, N. Li, X. Wu, S. Wang, S. Li, C. Guo, L. Yu, Z. Wang, P. Murto, X. Xu, Photothermal aerogel beads based on polysaccharides: controlled fabrication and hybrid applications in solar-powered interfacial evaporation, Water Remediat., Soil Enrich., ACS Appl. Mater. Interfaces 14 (2022) 50266–50279.
[33] B.C. Hodges, E.L. Cates, J.-H. Kim, Challenges and prospects of advanced oxidation water treatment processes using catalytic nanomaterials, Nat. Nanotechnol. 13 (2018) 642–650.
[34] M.-M. Wang, L.-J. Liu, J.-T. Wen, Y. Ding, J.-R. Xi, J.-C. Li, F.-Z. Lu, W.-K. Wang, J. Xu, Multimetallic CuCoNi oxide nanowires in situ grown on a nickel foam substrate catalyze persulfate activation via mediating electron transfer, Environ. Sci. Technol. 56 (2022) 12613–12624.
[35] A. Wang, J. Ni, W. Wang, X. Wang, D. Liu, Q. Zhu, MOF-derived N-doped ZnO carbon skeleton@hierarchical Bi_2MoO_6 S-scheme heterojunction for photodegradation of SMX: mechanism, pathways and DFT calculation, J. Hazard. Mater. 426 (2022), 128106.

[36] A. Wang, W. Wang, J. Ni, D. Liu, D. Liu, J. Ma, X. Jia, MOF derived ZnO clusters on ultrathin Bi_2MoO_6 yolk@shell reactor: establishing carrier transfer channel via PANI tandem S–scheme heterojunction, Appl. Catal. B: Environ. 328 (2023), 122492.
[37] H.-L. Wang, R.J. Romero, B.R. Mattes, Y. Zhu, M.J. Winokur, Effect of processing conditions on the properties of high molecular weight conductive polyaniline fiber, J. Polym. Sci. Part B: Polym. Phys. 38 (2000) 194–204.
[38] S. Chen, D. Huang, G. Zeng, W. Xue, L. Lei, P. Xu, R. Deng, J. Li, M. Cheng, In-situ synthesis of facet-dependent $BiVO_4/Ag_3PO_4$/PANI photocatalyst with enhanced visible-light-induced photocatalytic degradation performance: synergism of interfacial coupling and hole-transfer, Chem. Eng. J. 382 (2020), 122840.
[39] X. Liu, W. Zhou, F. Li, C. Yu, Eu^{3+} doped Bi_2MoO_6 nanosheets fabricated via hydrothermal-calcination route and their superior performance for aqueous volatile phenols removal, J. Taiwan Inst. Chem. Eng. 125 (2021) 276–284.
[40] X. Chen, J. Wang, Y. Chai, Z. Zhang, Y. Zhu, Efficient photocatalytic overall water splitting induced by the giant internal electric field of a g-C_3N_4/rGO/PDIP Z-scheme heterojunction, Adv. Mater. 33 (2021) 2007479.
[41] X. Meng, J. Yang, C. Zhang, Y. Fu, K. Li, M. Sun, X. Wang, C. Dong, B. Ma, Y. Ding, Light-Driven CO_2 reduction over prussian blue analogues as heterogeneous catalysts, ACS Catal. 12 (2022) 89–100.
[42] J. Wang, E. Kim, D.P. Kumar, A.P. Rangappa, Y. Kim, Y. Zhang, T.K. Kim, Highly durable and fully dispersed cobalt diatomic site catalysts for CO_2 photoreduction to CH_4, Angew. Chem. Int. Ed. 61 (2022), e202113044.
[43] L. Xia, K. Zhang, X. Wang, Q. Guo, Y. Wu, Y. Du, L. Zhang, J. Xia, H. Tang, X. Zhang, Y. Peng, Z. Li, X. Yang, 0D/2D Schottky junction synergies with 2D/2D S-scheme heterojunction strategy to achieve uniform separation of carriers in 0D/2D/2D quasi CNQDs/TCN/$ZnIn_2S_4$ towards photocatalytic remediating petroleum hydrocarbons polluted marine, Appl. Catal. B: Environ. 325 (2023), 122387.
[44] T. Feng, H. Yin, H. Jiang, X. Chai, X. Li, D. Li, J. Wu, X. Liu, B. Sun, Design and fabrication of polyaniline/Bi_2MoO_6 nanocomposites for enhanced visible-light-driven photocatalysis, N. J. Chem. 43 (2019) 9606–9613.
[45] L.J. Xu, W. Chu, L. Gan, Environmental application of graphene-based $CoFe_2O_4$ as an activator of peroxymonosulfate for the degradation of a plasticizer, Chem. Eng. J. 263 (2015) 435–443.
[46] S. Goberna-Ferrón, W.Y. Hernández, B. Rodríguez-García, J.R. Galán-Mascarós, Light-driven water oxidation with metal hexacyanometallate heterogeneous catalysts, ACS Catal. 4 (2014) 1637–1641.
[47] Y. Yamada, K. Oyama, T. Suenobu, S. Fukuzumi, Photocatalytic water oxidation by persulphate with a Ca^{2+} ion-incorporated polymeric cobalt cyanide complex affording O_2 with 200% quantum efficiency, Chem. Commun. 53 (2017) 3418–3421.
[48] Z. Wang, Y. Fang, Y. Yang, B. Qiu, H. Li, Vacancies-rich MOFs-derived magnetic CoFe encapsulated in N-doped carbon nanotubes as peroxymonosulfate activator for p-arsanilic acid removal, Chem. Eng. J. 454 (2023), 140474.
[49] W. Zhang, W. Huang, J. Jin, Y. Gan, S. Zhang, Oxygen-vacancy-mediated energy transfer for singlet oxygen generation by diketone-anchored MIL-125, Appl. Catal. B: Environ. 292 (2021), 120197.
[50] M. Kohantorabi, S. Giannakis, G. Moussavi, M. Bensimon, M.R. Gholami, C. Pulgarin, An innovative, highly stable Ag/ZIF-67@GO nanocomposite with exceptional peroxymonosulfate (PMS) activation efficacy, for the destruction of chemical and microbiological contaminants under visible light, J. Hazard. Mater. 413 (2021), 125308.
[51] J. Jia, D. Liu, J. Tian, W. Wang, J. Ni, X. Wang, Visible-light-excited humic acid for peroxymonosulfate activation to degrade bisphenol A, Chem. Eng. J. 400 (2020), 125853.
[52] X. Sun, H. Qi, S. Mao, Z. Sun, Atrazine removal by peroxymonosulfate activated with magnetic CoFe alloy@N-doped graphitic carbon encapsulated in chitosan carbonized microspheres, Chem. Eng. J. 423 (2021), 130169.
[53] J. Ni, Z. Wei, A. Wang, D. Liu, W. Wang, X. Song, Z. Xing, Nano cocatalyst–catalytic system for boosting photothermal–photocatalytic water treatment enabled by visible LEDs, Environ. Sci. Nano 10 (2023) 1778–1789.
[54] Z. Wu, X. Wang, J. Qiu, C. Liu, Z. Yu, J. Zhang, Z. Qiu, In-situ uniform growth of ZIF-8 on 3D flower-like NiCoLDH microspheres to enhance tetracycline and doxycycline removal from wastewater: Anti-interference and stability tests, Sep. Purif. Technol. 302 (2022), 122078.
[55] N. Li, R. Li, X. Duan, B. Yan, W. Liu, Z. Cheng, G. Chen, La Hou, S. Wang, Correlation of active sites to generated reactive species and degradation routes of organics in peroxymonosulfate activation by Co-loaded carbon, Environ. Sci. Technol. 55 (2021) 16163–16174.
[56] Z. Zhang, Z. Pan, Y. Guo, P.K. Wong, X. Zhou, R. Bai, In-situ growth of all-solid Z-scheme heterojunction photocatalyst of $Bi_7O_9I_3$/g-C_3N_4 and high efficient degradation of antibiotic under visible light, Appl. Catal. B: Environ. 261 (2020), 118212.